Chapter 2

Outline of Observational Data and Analysis Tools

In this chapter, we outline many observatories and their instruments whose data we have utilized for our research presented in this thesis. We used data from the space-based observatories Interface Region Imaging Spectrograph (IRIS) and Solar Dynamic Observatory (SDO) to study the physics of waves in the solar atmosphere. We used spectroscopy data from IRIS taken in the sit-n-stare mode. The magnetogram observations from Helioseismic Magnetic Imager (HMI) onboard SDO is also utilized to determine the network and inter-network area boundaries in the quiet-sun. We also studied sunspot umbral oscillations using data from the Goode Solar Telescope (GST) deployed at the ground-based observatory Big Bear Solar Observatory (BBSO). For the investigation of quasi-periodic pulsations, we used the imaging observations from Atmospheric Imaging Assembly (AIA) onboard SDO, and spectrosopic data in form of raster scan from IRIS. We discuss about a variety of analysis methods that were employed to examine these observational data sets, including wavelet analysis, differential emis-

sion measure (DEM), spectral analysis, image calibration, and study of the magnetogram data.

2.1 Introduction

A thorough understanding of the physics behind the many dynamical plasma processes in the solar environment requires an analysis of the observational data that includes imaging, spectroscopic, spectropolarimetric, and magnetic field measurements (e.g., Curdt et al., 2001; De Pontieu et al., 2014, 2022; Del Zanna and Mason, 2018; Hinode Review Team et al., 2019; Iglesias and Feller, 2019; Jess et al., 2015; Stenflo, 2013; Tziotziou et al., 2023; Wilhelm et al., 2007, and references cited therein). The sun's atmosphere is made up of multiple layers. The solar surface (photosphere) can be viewed at the visible wavelengths. As a result, ground-based observatories such as BBSO SST and DKIST are suited for observing the photosphere since they give observations in visible wavelength bands. However, the upper layers emit lights in the UV/EUV and X-ray wavelength range, therefore space-based observatories are needed to capture the upper layer as UV/EUV does not reach through earth's lower atmosphere at the ground. However, space instruments can observe the sun at a variety of wavelengths across the electromagnetic spectrum. Each wavelength reveals information on different aspects of the solar atmosphere. For example, The Solar Dynamics Observatory (SDO) (Pesnell et al., 2012) uses its Atmospheric Imaging Assembly (AIA) telescope with 10 different filters to observe the solar atmosphere in the Extreme Ultraviolet and UV continuum. These filters correspond to different solar temperatures, allowing for extraction of information from plasmas in different layers of solar atmosphere. The Helioseismic and Magnetic Imager (HMI) onboard SDO monitors

the sun's surface and magnetic field, providing valuable information about its magnetism (see Figure 2.1).

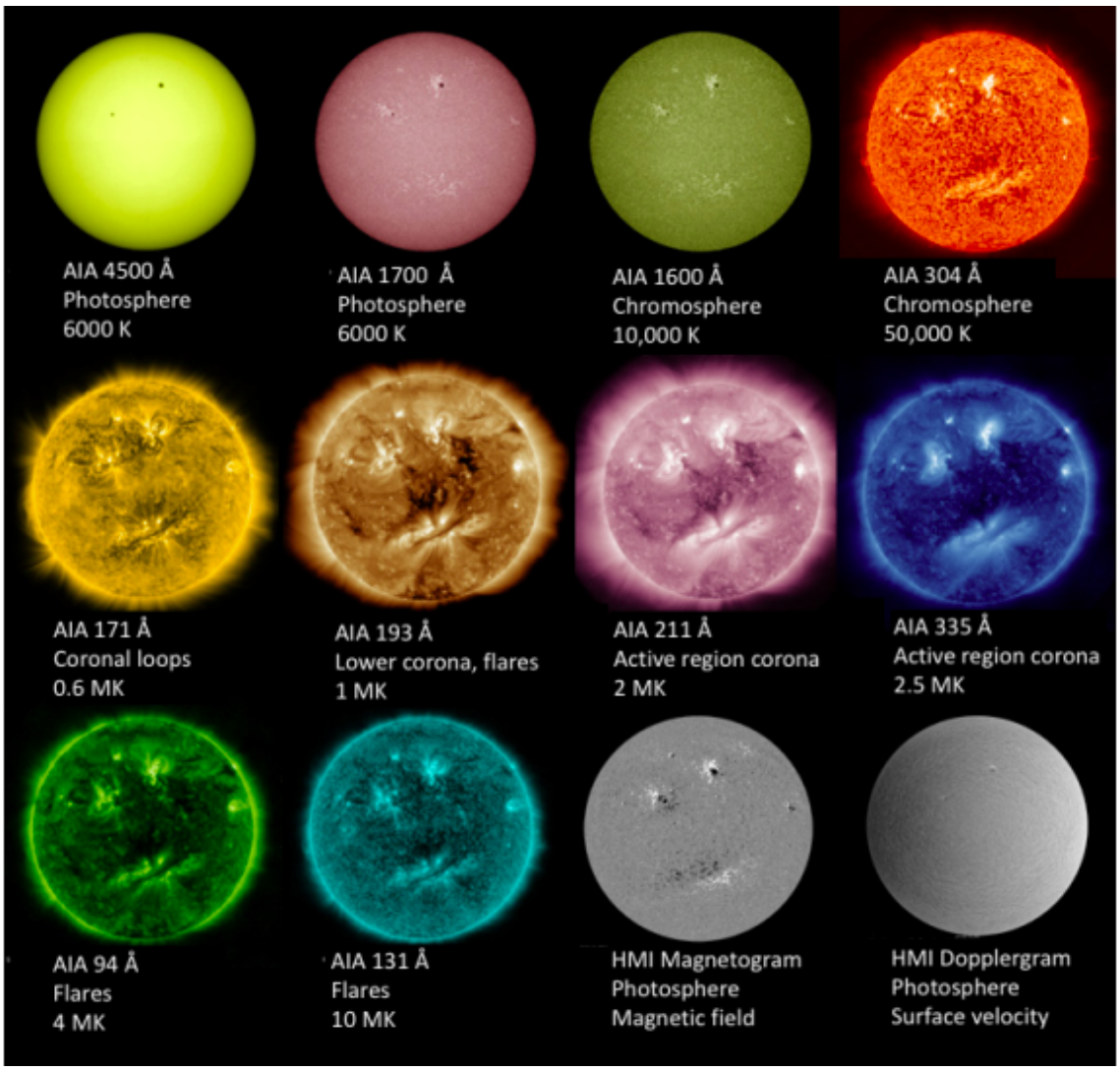

Figure 2.1: Sun viewed at various wavelengths measured by SDO. Different wavelengths of the sun's observation aid in highlighting various features of the sun's surface and atmosphere. The first 10 images are taken from Atmospheric Imaging Assembly (AIA), while the last two images are from the Helioseismic and Magnetic Imager (HMI) showing magnetogram, and dopplergram (Credit: NASA/SDO and AIA and HMI science teams).

The high energy dynamical plasma events, e.g., solar jets, flares, magnetic reconnection, waves, etc. that occur in the magnetised and structured atmosphere of the sun can be studied using emissions detected in the EUV, soft and hard X-ray (e.g., De Moortel

and Nakariakov, 2012; Graham et al., 2020; Jess et al., 2023; Raouafi et al., 2016; Shibata and Magara, 2011, and the cited references therein). Using EUV and X-ray emissions, a number of physical processes that may be responsible for the waves, localised mass transfer and coronal heating are diagnosed. Most UV/EUV emissions indicate that the various ions generated at temperatures between 10,000 K and 20 MK (e.g., Del Zanna and Mason, 2018; Wilhelm et al., 2004). And these ions will emit the UV/EUV spectral lines and these spectral lines helps us in diagonistic upper atmosphere comprises chromosphere, transition region, corona (e.g., Brooks et al., 2011; Tian, 2017, and the cited references therein). The solar corona is mostly constituted of highly ionised species and elements, whereas the lower solar atmosphere (photosphere and chromosphere) is composed of ions, electrons, and neutrals due to the lower temperature. Furthermore, continuous emissions and atomic lines are produced by the colder regions of the solar atmosphere, which are located below the temperature minimum and between the photosphere and chromosphere. Because these atomic radiations are vulnerable to the surface magnetic fields, magnetograms or spectropolarimetric observations aid in their analysis. As a result, we can study many physical processes (e.g., heating, waves dynamics etc) occurring in the plasma by combining observations of spectroscopy, imaging, and magnetic/spectropolarimetric data. Joint observations from ground and space-based telescopes enable the simultaneous acquisition of data for solar plasma and magnetic feild diagnostics. The understanding of intricate magnetic field structure, such as flux-emerging regions, active regions/sunspot regions, network/inter-network regions etc., is also aided by these data.

This thesis describes original research that has been done to better comprehend waves and quasi-periodic pulsations in the solar atmosphere. Spectral lines from various ions as observed by IRIS from the photosphere to the transitional region are used to understand the dynamics of the waves, their propagation, and physical nature in multiple layers of the solar atmosphere (chapter 3 and chapter 4). Additionally, we have estimate the strength

and inclination of the magnetic field for the studied solar region using the magnetogram data from SDO/HMI. We have also analyzed the umbral oscillation of the sunspot using observations from the GST/BBSO observatory (chapter 5). We have used spectral data from IRIS and image data from AIA onboard SDO to investigate the origin of quasi periodic pulsations (chapter 6). We have used a variety of analysis methods to retrieve the physical information from these informations. In this chapter, the various observational instruments and analyses techniques are presented. Different instruments are addressed in section 2.2. Data reduction and analyse methods are described in section 2.2 and 2.3 respectively.

2.2 Space-Based Observatories

In this section, we discuss the observatories and their instruments, whose data was used in this thesis. We also discuss about the various analysis techniques used to derive scientific and physical information from different data sets.

2.2.1 Interface Region Imaging Spectrograph (IRIS)

Table 2.1: IRIS observations in different passband, corresponding emitting ions, and temperature (Credit: LMSAL, NASA/IRIS).

Pass band	Wavelengths (Å)	Ions	FOV (″×″)	log T
NUV	2820	Mg II wing	175 × 175	3.7-3.9
FUV 1	1355.6	O I	175 × 175	3.8
NUV	2803.5/ 2796.4	Mg II h/ Mg II k	175× 175	4.0
FUV 1	1334.5/ 1335.7	C II/ C II	175× 175	4.3
FUV 2	1402.8/ 1393.8	Si IV/ Si IV	175× 175	4.8
FUV 2	1399.8/ 1401.2	O IV/ O IV	175× 175	5.2
FUV 1	1349.4	Fe XII	175× 175	6.2
FUV 1	1354.1	Fe XXI	175× 175	7.0

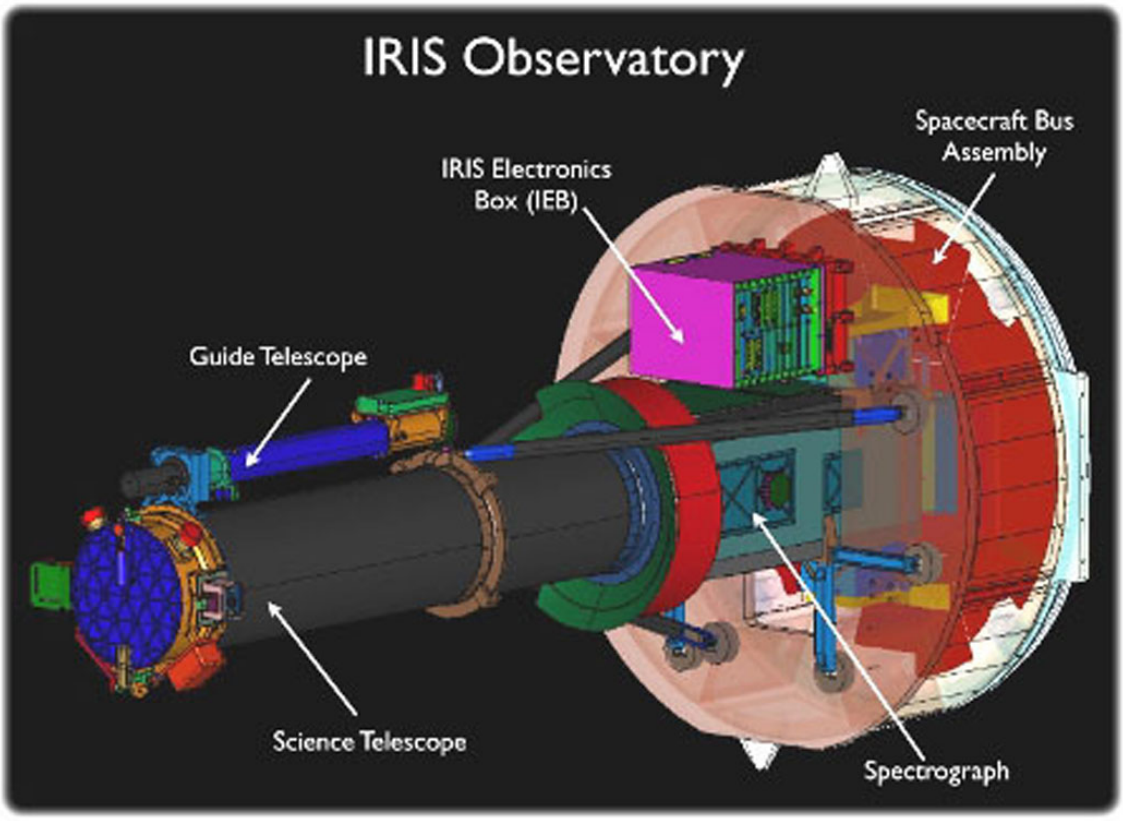

Figure 2.2: Image showing the Interface Region Imaging Spectrograph (IRIS) (Credit: LMSAL, NASA/IRIS)

.

The Interface Region Imaging Spectrograph [1] (IRIS, De Pontieu et al., 2014, 2021), see Figure 2.2) is a space-based telescope funded by NASA's Small Explorer program and launched on June 13, 2013. Since then, it has provided data in the UV wavelength range. It is primarily intended to examine the chromosphere and transition region, with the main scientific goal of understanding the energetics of the solar atmosphere. It has a 19 centimeter telescope and can perform imaging as well as spectroscopic studies. It primarily comprises of a slit spectrograph for spectroscopic data and a slit jaw imager for imaging data. It features a spatial resolution of 0.33-0.4 $''$, a time resolution of 1 second, and a spectral resolution of 26 mÅ for FUV and 53 mÅ for NUV. It produces simultaneous

[1] http://iris.lmsal.com/data.html

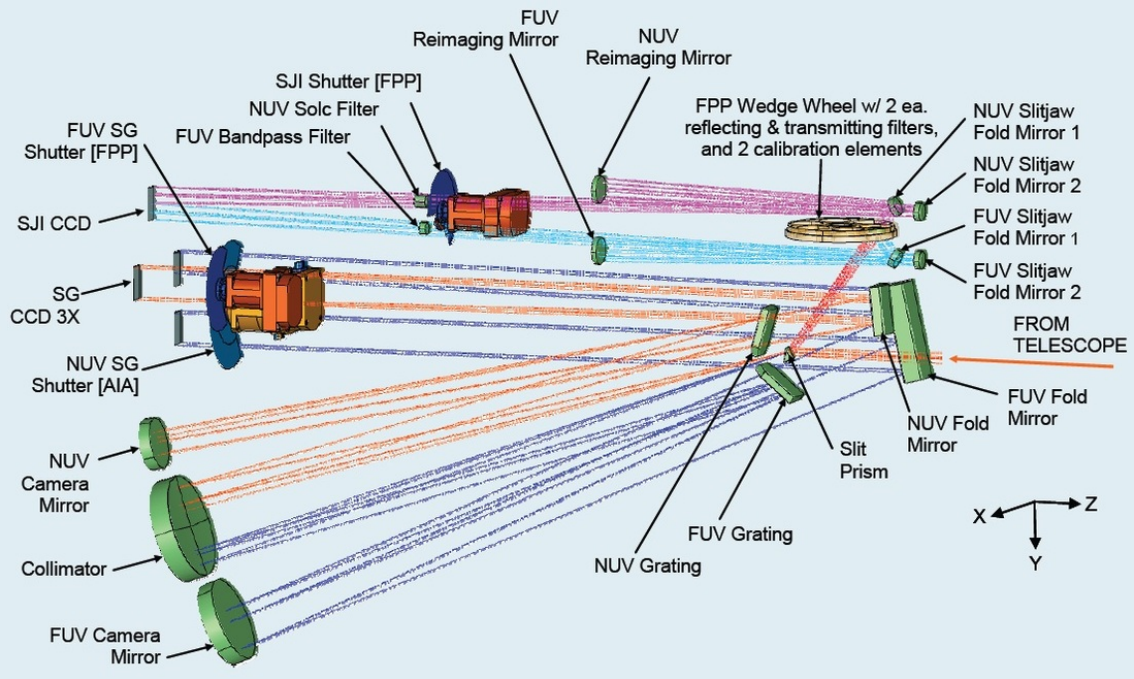

Figure 2.3: Diagram describing the direction of the light traces its path in the Spectrograph and slit-jaw imager (Credit: LMSAL, NASA/IRIS)

.

UV spectra and images from photosphere to the transition regin over a field of view of $175'' \times 175''$. Figure 2.3 shows a schematic depiction of both the slit-jaw imager and the spectrograph. It demonstrates incoming light from the telescope falling on the prism. The rays of light directs to the SJI and the slit, which is dispersed first before being directed to the collimator mirror. The dispersed light breaks into FUV and NUV components. These two beams are subsequently delivered to different CCDs. The spectrograph acquires spectral data in two modes. The first is the sit-and-stare mode, where the slit remains stationary and the telescope continuously observes a single point. This mode is suitable for studying wave dynamics in the solar atmosphere. The second mode is the raster mode, in which the slit scans across the solar disk with step sizes of $0.33''$ (dense), $1''$ (sparse), and $2''$ (coarse). The slit collects spectra in different passband, i.e., FUV and NUV. The FUV offers spectral data in two windows, e.g., 1331-1358 Å and 1380-1406 Å. The NUV

gives spectral data from 2783-2835 Å. The Slit Jaw Imager (SJI) captures images in four passbands, i.e., Mg II wing 2830 Å, Mg II K 2796 Å, Si IV 1400 Å, and C II 1330 Å.

The strongest spectral lines observed by the IRIS spectrograph are Mg II h 2803 Å, Mg II k 2796 Å, C II 1334/1335 Å, and Si IV 1394/1403 Å. It also observes photopshric spectral lines located in the wings of NUV spectral window. Every line is formed at a different temperature. Table 2.1 showed the rest wavelength, associated ions, and formation temperature. The formation temperature of these lines ranges from 6000 and 80,000 K. Table 2.1 shows that distinct spectral lines form at different atmospheric heights. Consequently, by examining different spectral lines formed at various heights in the solar atmosphere, such as the photosphere, chromosphere, and transition region, we can perform a comprehensive scan of these layers simultaneously. In Chapter 4, we analyzed these spectral lines to explore the physics of wave propagation in the solar atmosphere. Chapter 3 focuses on the transition region's Si IV 1393.755 Å spectral line, where we calculated the physical characteristics of oscillations in this region. The IRIS mission, which targets the chromosphere and transition region, provides insights into the non-thermal energy sources that heat the solar chromosphere or corona and contribute to the solar wind. Additionally, IRIS observations offer spectroscopic diagnostics of the solar plasma, supplying information on velocity, non-thermal energy, density, and turbulence. In this thesis, we utilized sit-and-stare data to gain a deeper understanding of wave dynamics in the solar atmosphere.

2.2.2 Solar Dynamics Observatory (SDO)

The Solar Dynamics Observatory (SDO), a NASA space mission, was launched on February 11, 2010, and commenced providing observational data from May 1, 2010, onward (Pesnell et al., 2012). The primary scientific goal of SDO is to investigate the dynamics of the solar atmosphere and its interaction with Earth's atmosphere. Furthermore, it seeks to

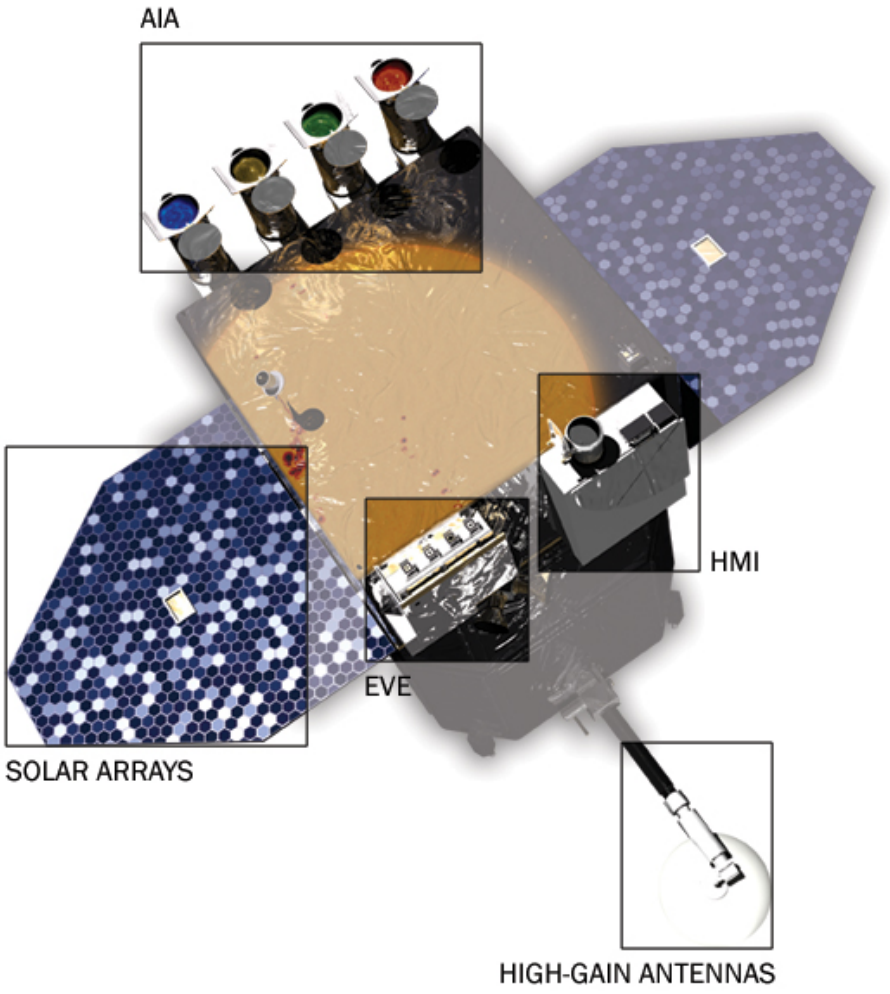

Figure 2.4: A diagram of the Solar Dynamics Observatory (SDO) spacecraft showing three payloads i.e., AIA, HMI, and EVE (Credit: NASA/SDO).

uncover new information about the physical mechanisms driving the release of magnetic energy into the heliosphere and to measure the magnetic field strength at the photosphere.

As shown in Figure 2.4, SDO is equipped with three main payloads, namely, the Helioseismic and Magnetic Imager (HMI), the Extreme Ultraviolet Variability Experiment (EVE), and the Atmospheric Imaging Assembly (AIA). With a 28-degree inclination with respect to the longitudinal plane of the ground station in New Mexico, USA, it was

launched into a geosynchronous orbit. Although initially designed for a five-year mission, SDO is still operating and supplying valuable data for over a decade.

SDO captures the high-resolution images, to study the transients event such as CMEs, prominence eruption, flares etc. These images are captured using a CCD with a dimension of 4096 pixel × 4096 pixel. This thesis utilizes data from the AIA and HMI instruments. The subsequent sub-section will delve into the distinctive features of AIA and HMI, as the data from these instruments serve important role in the research described in this thesis.

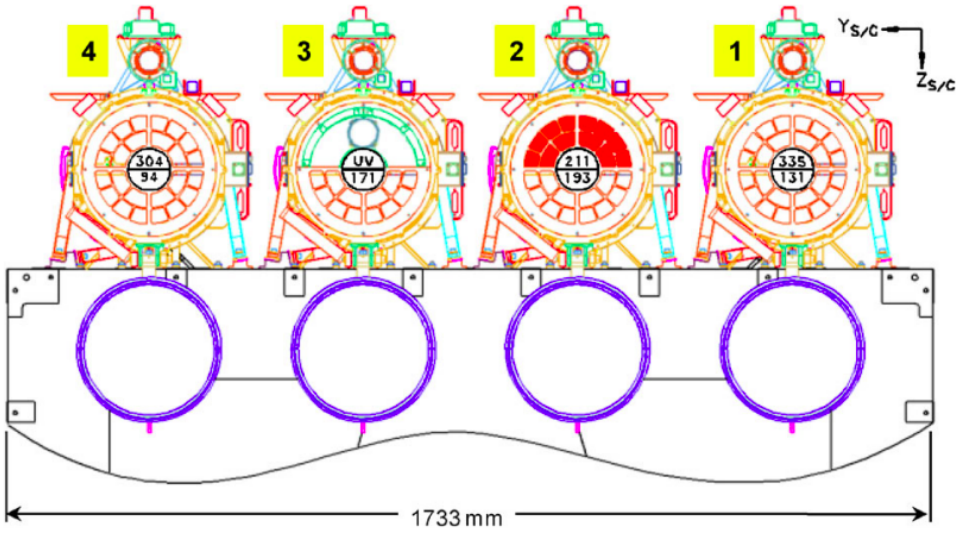

Figure 2.5: A visual representation of the AIA showing the four telescopes (Credit: Lemen et al., 2012).

Atmospheric Imaging Assembly (AIA)

The AIA consists of four telescopes that are used to monitor the solar atmosphere in two ultraviolet (UV) bands, one visible light band, and seven extreme ultraviolet (EUV) bands (e.g., Pesnell et al., 2012). Each telescope has its unique configuration, as shown in the cross-sectional view in Figure 2.5. While three telescopes feature mirrors for two distinct EUV band passes, the fourth includes a 171 Å band pass on one half and a broad-band UV coating on the other. It primarily focuses on the iron lines listed in table 2.2. It employs optics coated with multiple layers to capture narrow-band images in seven EUV bandpasses.

Table 2.2: The details of Primary Ions and Their Characteristic Temperature Corresponding to Different Filters of AIA (Credit: NASA/SDO, Lemen et al. 2012)

Primary ion(s)	log T	Channel	Region of Sun's atmosphere
continuum	3.7	4500 Å	photosphere
continuum	3.7	1700 Å	temperature minimum, photosphere
continuum, C IV	5.0	1600 Å	upper photosphere, transition region
He II	4.7	304Å	chromosphere, transition region
Fe IX	5.8	171 Å	quiet corona, upper transition region
Fe VIII, XXI	5.6, 7.0	131 Å	transition region, flaring corona
Fe XII, XXIV	6.3, 7.3	193 Å	corona and hot flare plasma
Fe XIV	6.3	211 Å	active-region corona
Fe XVI	6.4	335 Å	active-region corona
Fe XVIII	6.8	94 Å	flaring corona

A different telescope uses a visible light filter to coordinate its observations with those of the other telescopes as it views C IV (around 1600 Å) and the nearby continuum (1700 Å). AIA features a 0.6 arcsec spatial resolution and varies its temporal resolution depending on the filter. The temporal cadence for EUV filters is 12 seconds, while the temporal cadence for UV filters is 24 seconds. The AIA instrument provides a full disc image of the sun, from which we can extract observations of its subregions based on the region of interest. Table 2.2 outlines the primary plasma components and their characteristic temperatures as observed by different filters (e.g., Lemen et al., 2012).

Helioseismic and Magnetic Imager (HMI)

Measurements of vector magnetic fileds, intensties, and Doppler shifts in the photosphere are made using the vector magnetograph Helioseismic and Magnetic Imager (HMI) (e.g., Scherrer et al., 2012). Observations from Fe I 6173 Å absorption line are used to measure these quantities using spectral and polarimetric techniques (e.g., Schou et al., 2012). The HMI instrument is equipped with a variety of components, including a telescope, filters, waveplates, and interferometers, along with two CCD cameras (refer to Figure 2.6). It captures full-disk images every 45 seconds, providing detailed information

on intensity, magnetic field strength, and Doppler velocity. Operating at a spatial resolution of 0.5″, HMI offers various data outputs, including Velocity Dopplergrams, continuum filtergrams, and magnetograms, which help us to understand the magnetic fields within the solar photosphere. By analyzing the line-of-sight magnetic field in the photosphere, we can estimate the magnetic field in the solar corona.

The major scientific objective of HMI is to understand more about the internal structure of the sun and the factors that drive solar variability. Magnetic field lines are observed by the HMI to be emerging from the solar interior. These new magnetic field lines would interact with the existing polarity, perhaps leading to transient processes such as eruptions. HMI investigates solar oscillations and tracks the movement of the solar photosphere. By measuring the polarization of specific spectral lines, HMI provides valuable information about the magnetic field on the sun's surface. Utilizing measurements of the photospheric magnetic field, we delineated the boundary between network and inter-network regions. Our observations, particularly in Chapter 3 and 4, focus on the quiet-sun and utilize magnetic field measurements to distinguish between network and inter-network regions.

2.2.3 Big Bear Solar Observatory (BBSO)

Big Bear Solar Observatory (BBSO), located in the United States, is a ground-based solar observatory operated by the New Jersey Institute of Technology (NJIT). Equipped with advanced instruments and telescopes, BBSO specializes in providing high-resolution observations of the solar photosphere and chromosphere. These observations are crucial for studying various activities and phenomena on the sun. The Goode Solar Telescope (GST) at BBSO holds the distinction of being the world's second-largest solar telescope, following the Daniel K. Inouye Solar Telescope (DKIST) (see, Figure 2.7). The primary mirror of the GST is 1.6 meters off-axis, which has the benefit of eliminating light diffraction from the secondary mirror (e.g., Cao et al., 2010). The active optics and 308

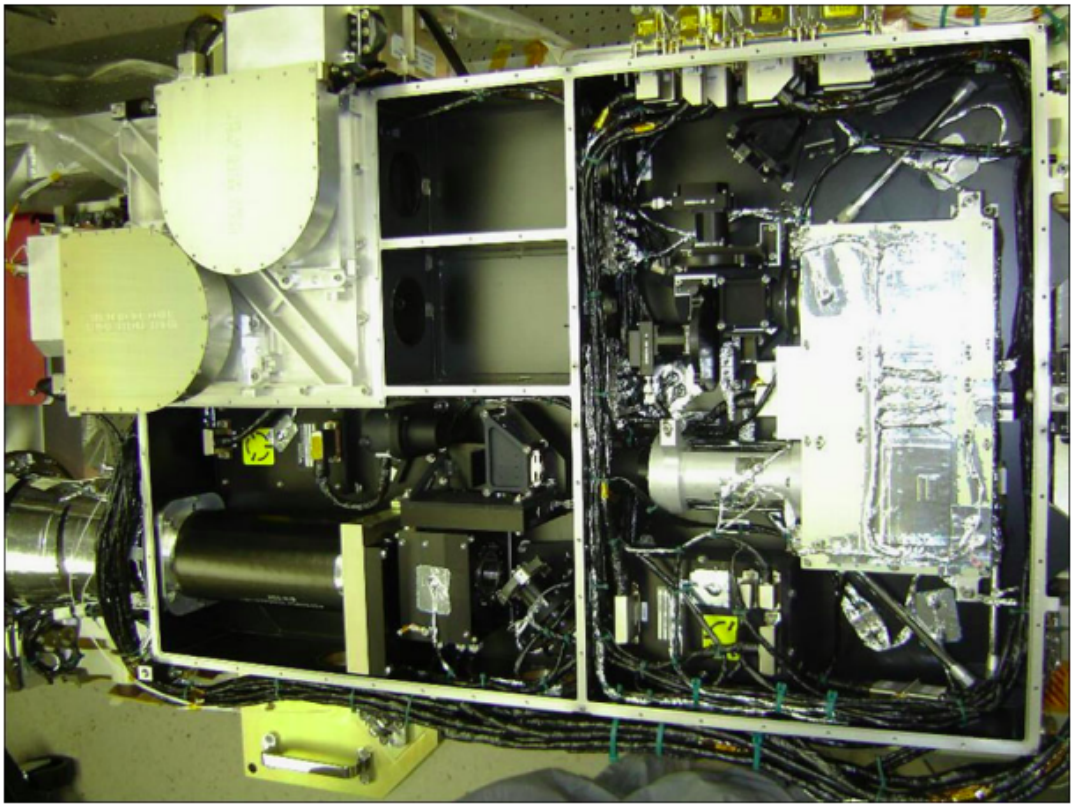

Figure 2.6: Image showing HMI onboard SDO (Credit: Schou et al., 2012).

sub-aperture adaptive optics added to give diffraction limited images considerably improve its performance. It was designed to study the chromospheric dynamics using both the Hα and Ca II 8542 Å lines. The resolution of the GST is 0.2″ at 1.56 μm and 0.06″ at 0.5 μm. A maximum square field of vision (FOV) measuring 70″ by 70″ is defined by the 100 circular openings in the field. For diffraction-limited imaging, the GST features a nearly achromatic, fully functional AO system in the laboratory mounted on a vertical bench. Because of AO system constraints, early observations were primarily conducted in the near infrared (NIR) range. These limitations are gradually being addressed by bigger format deformable mirrors (DMs). The post-focus instrumentation includes a a visible imaging spectrometer (VIS), a fast-imaging solar spectrograph (FISS), broadband filter image (BFI), a near-infrared imaging spectropolarimeter (NIRIS), and a cryogenic infrared

spectrograph (CYRA). The location also houses an Hα full-disk imager that is part of the Global Hα Network, as well as a Global Oscillations Network Group (GONG) station. We used the Hα data from the Visible Imaging Spectrometer (VIS) in this thesis.

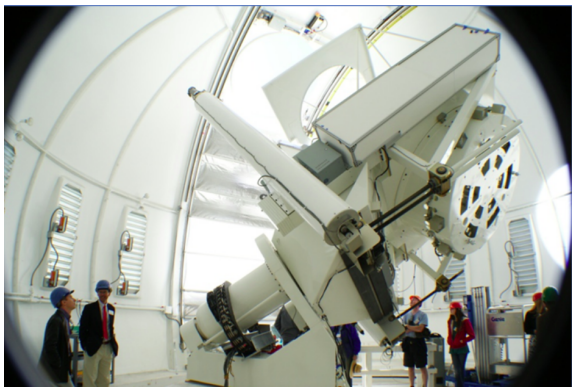

Figure 2.7: Image showing GST installed at BBSO Observatory (Credit: BBSO/NJIT).

Visible Imaging Spectrometer (VIS)

Visible imaging spectrometer (VIS) is designed to give spectral diagnostics of solar phenomena at the telescope's diffraction limit. VIS presently produces a narrow 0.07 Å bandpass across a 70″ circular field of view by adapting a single Fabry-Pérot etalon. The wavelength range varies from 5500 Å to 7000 Å. The upgrade of VIS to a dual-etalon system is planned in the future. The available spectral lines are Hα, Fe I at 6300 Å, and Na I D2 at 5890 Å. The He I D3 line at 5876 Å will soon be introduced. The 11 line locations are sampled in 15 seconds, with the image scale being 0.034″/pixel. There is a configurable parameter that controls the quantity of line positions and the associated temporal resolution. In order to recreate speckle at each line point, bursts of usually 25 frames are used.

2.3 Data Reduction Pipeline

Calibration is required to produce high-quality scientific data. In this section, we will provide an overview of the image reduction pipeline and spectra reduction used to extract data files from observational data, which will then be evaluated using the data analysis methodologies outlined in the following sub-section.

2.3.1 Spectral analysis

We used IRIS spectral data in chapters 3-5 to study the origin and physical properties of the waves in the solar atmosphere. IRIS delivers data at several wavelengths, allowing for full observations from the photosphere to the chromosphere and transition region. Photospheric lines are absorption lines. The photosphere is visible using spectral lines such as Fe I 2799.972 Å, Ni I 2805.904 Å, and Mn I 2801.907 Å. These lines represent an inverted Gaussian profile. The chromosphere is distinguished by a strong Mg II k 2795.528 Å, and Mg II h 2802.704 Å lines, which is an optically thick emission line. The transition region can be seen through the Si IV 1393.755 Å / 1402.770 Å, and C II 1335 Å lines. Si IV is an optically thin emission line with a Gaussian shape. The C II 1335 Å line is an optically thick emission line. The first step in spectroscopy is to determine spectral characteristics like intensity and Doppler velocity over various time intervals to create time-series that depict the evolution of physical parameters over time. We utilize multiple fitting functions for different spectral lines to determine intensity and Doppler shift at different spatial locations and times. Intensity represents the amount of plasma being emitted, whereas Doppler shift represents plasma velocity along the line of sight. In the case of a positive Gaussian profile, we utilize the positive Gaussian function; for an inverse Gaussian profile, we use the negative Gaussian function. For double Gaussian profiles, we employ a mixture of positive and negative Gaussian functions. Also the estimation of the value of rest wavelength is critical for measuring Doppler shift accurately. To determine

Doppler velocities precisely, we used the shift in cool lines Ni I 2799.474 Å and S I 1392 Å measured during a typical quiet-sun.

Mg II h&k lines have single, double, or many peaks depending on the *in-situ* plasma state (e.g., Leenaarts et al., 2013a). For instance, Tian et al. (2014a) reported a single gaussian profile in sunspots. But in the quiet-sun region, it primarily displays a double Gaussian profile, with two peaks i.e.,k_{2V} and k_{2R} originating from the middle chromosphere and a dip i.e., k3 from the top chromosphere. These two peaks are the most noticeable in the IRIS NUV spectral range. They encompass a wide spectrum of solar atmosphere formation heights. The Mg II h&k line can be analyzed using the built-in procedure iris_get_mg_features_lev2.pro (e.g., Pereira et al., 2013). However, we employed a combination of positive and negative Gaussian functions as described in Schmit et al. (2015). We measured the Doppler velocities of the k3 dip of Mg II at 2803.52 Å lines. They employed polynomials to fit the background, whereas we used linear lines. In chapters 3 and 4, we used sit-and-stare data to explore the dynamics of the waves in the solar atmosphere. First, we need a time-series of intensity and velocity. Sit-and-stare data includes spectra at each 'y' for several time steps. Assume there are 100 time steps for each 'y'. Then we computed I and V for each time step that correspond to a given 'y'-pixel. As a result, time-series for I and V are calculated for each 'y' point. To estimate the periodicity and physical character of the time-series, we used wavelet and cross-wavelet tools, along with the implication of a generic noise model, which is explained in the next section.

2.3.2 Image calibration and data processing

Utilizing image data from AIA, we were able to comprehend the dynamics of solar environment and its plasma processes. AIA images are available in level 1.5 format and are already flat-fielded, rebinned, and processed to eliminate spikes and poor pixels. Further

information regarding the AIA data-product is available in Lemen et al. (2012). For the analysis of AIA data products, we have used procedures included in Solar Soft package (e.g., Freeland and Handy, 1998). The keyword contains the attributes, which include the center coordinates, pixel size, and number of pixels in the 'x' and 'y' directions. Using these keywords, one or more images can be co-aligned using the image calibration methods i.e., aia_prep.pro. Every keyword in the header of image file is modified to match with the reference image, which serves as the alignment point for all other images. Additionally, it aligns images with varying spatial resolutions that were taken with various instruments. For easy comprehension and examination, the AIA images can be scaled, resized, and color contrasted. These processed data sets are then subjected to various analytical techniques in order to obtain a scientific results depicting the physical phenomenon occurring in the localized solar atmosphere as observed by the particular data set.

2.3.3 Analysis techniques of magnetogram data

Similar to the other AIA data products, the LOS magnetograms are available in level 1.5 format and have previously been flat-fielded, rebinned, and treated to remove spikes and bad pixels. However, due to the inherent complexity of the solar magnetic field in space and time, it exhibits problems with instrumental qualities such as scattered light, spatial resolution, and filter properties. As a result, image rotation is required, and the data set is subsequently processed using the hmi_prep.pro routine. To improve co-alignment, HMI data are calibrated and aligned using AIA 1600 Å filter. Vector magnetograms offer three components of the magnetic field, namely, field strength B_r, field inclination B_θ, and azimuth B_ϕ. These components can be utilized for extrapolation and inversion to acquire information about physical quantities. The inversion creates a 180° ambiguity in the azimuthal field direction. The potential-field method, random method, and radial acute angle method are utilized to resolve this ambiguity, which is then used to complete the

subsequent analysis to obtain physical information. The details of HMI data, its acquisition, callibrations, and analysis are described in Scherrer et al. (2012) and Schou et al. (2012).

2.3.4 Chromospheric observations by VIS on BBSO telescope (GST)

The Visible Imaging Spectrometer investigated the sunspot region at Hα 6,563 Å. The scanning was conducted at intervals of 0.2 Å, covering the blue wing (1.0 Å) to the red wing (1.0 Å). Using speckle imaging techniques, each image was recreated. The observational dataset was reconstructed to be suitable for capturing fine-scale plasma dynamics by eliminating targeting errors resulting from air turbulence. We used these datasets in chapter 6 of this thesis to understand the wave propagation above sunspots.

2.4 Data Analysis Techniques

This section provides a brief overview of the data analysis methods that we use to calibrate the data and extract different metrics and features of the dynamical plasma processes occuring in the localised solar atmosphere.

2.4.1 Differential emission measure (DEM) analysis

A variety of solar atmospheric emissions encompass a wide range of plasma temperatures. Hence, there is a broad spectrum of thermally balanced and optically thin UV/EUV emissions from the solar atmosphere. The density and temperature structure of the multi-thermal plasma in the sun's atmosphere can be ascertained by the use of a technique called DEM. The DEM is stated as (Cheung et al., 2015):

$$DEM(T) = \int n_e^2(h(t))\frac{dh}{dT} \tag{2.1}$$

where $n(h(T))$ shows the electron density at temperature T at a depth of h, and $DEM(T)$ represents the DEM at a plasma temperature $'T'$ and at a depth of $'h'$ along the line-of-sight. Generally speaking, DEM can be carried out by applying a variety of strategies/methods (e.g., Regularized Inversion Method, Sparse Inversion Method, etc) to predict the temperature and density structures of plasma appearing in different transients and eruptive events. Understanding the thermal nature of the transient jet be facilitated by utilising the DEM parameter, as discussed in Chapter 6. We used the technique established by (Hannah and Kontar, 2012) to estimate the DEM. The DEM is produced by this method using the warm/hot EUV channel of AIA/SDO (e.g., 94, 131, 171, 193, 211, and 335 Å) and a regularised inversion algorithm. This automated technique, known as zeroth-order regularised inversion, generates the DEM as a function of temperature. The generated DEM has a positive solution thanks to this regularised approach. The details of DEM as employed on the observed AIA data set and associated physical information are described in chapter 6.

2.4.2 Wavelet analysis technique

The wavelet analysis [2] is a well-known approach for estimating periodicities in time-series (Torrence and Compo, 1998). This approach shows how the power of a time-series varies across different frequencies and over time. Unlike the Fourier transform, which only analyses frequencies, wavelet analysis takes into account frequency and time, offering more complete information about the oscillatory pattern. The time-series is convolutioned with the "mother" function to create the wavelet transform. A multitude of mother functions, such as Paul, Morlet, and derivative of Gaussian (DOG), are covered in

$$\psi_0(\eta) = \pi^{-1/4} e^{i\omega_o \eta} e^{-\eta^2/2} \tag{2.2}$$

[2] https://paos.colorado.edu/research/wavelets/

DOG functions provide real transformations and hence are unsuitable for phase analysis, whereas Paul functions are more suited for pulse changing research since they are more specified in time. In Chapters 3-5, we wanted to perform phase analysis, and we needed to know both the real and imaginary parts of the wavelet transformation, so we utilized the Morlet function, which offers both amplitude and phase information. For a time-series, the wavelet transform yields a 2D complex array. The square of the absolute magnitude of the complex wavelet is known as the wavelet power. Since smoothing might introduce erroneous periodicities into the time-series, we chose not to detrend it before applying the wavelet transform (e.g., Auchère et al., 2016).

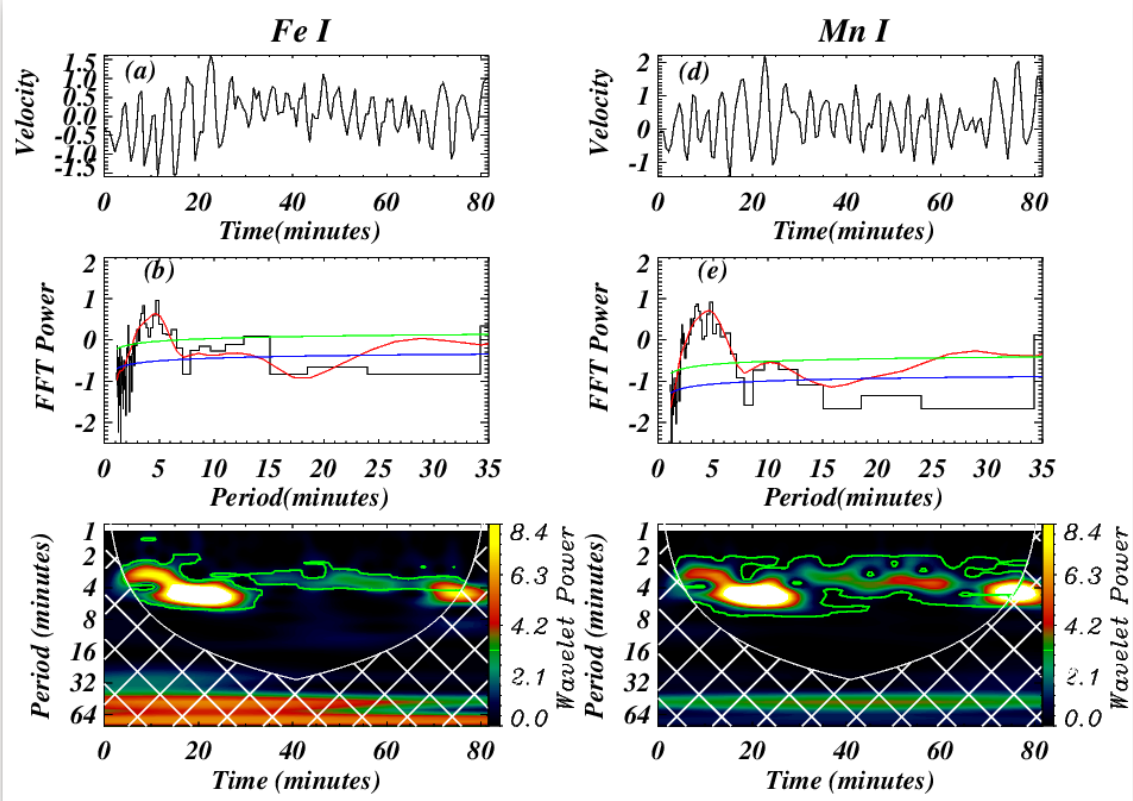

Figure 2.8: Image showing an example of wavelet analysis. Details are given in Chapter 4.

Figure 2.8 shows the example of wavelet power spectrum (panel 'c' and panel 'f'). The more details of such time-series derived from IRIS observations, their wavelet analysis are described in chapter 4. Here, we aim to just demonstrate various features of the

wavelet power spectrum. The cone of influence, depicted by the white cross-hatched area, disregards power measurements within it because edge effects render them statistically insignificant (Torrence and Compo, 1998). The significance level contour needs to be created in order to guarantee the accuracy of the power that was collected. According to Torrence and Compo (1998), the most popular noise models for determining significant levels are the red and white noise models. These models, however, sometimes mislead the magnitude of the observed power (e.g., Auchère et al., 2016). In order to determine the significance level, we have used the power law noise model rather than these conventional noise models. The power law noise model was first presented by Auchère et al. (2016), and it has since been employed in various analyses in the past (Kayshap et al., 2020; Threlfall et al., 2017).

Power law Noise Model

The power law noise equation is given as (Auchère et al., 2016)

$$\sigma(\nu) = A\nu^{s} + C \tag{2.3}$$

The first term is the power law function with 'A' is constant, ν is frequency. The second term 'C' is a constant. Each power spectrum has been fitted with the $\sigma(\nu)$ function. The fitted power law noise model is shown by the blue curve in panels (b) and (e) of Figure 2.8, whereas the black curve represents the time-series power spectrum. We used the fitted curve as the background model and estimated the 95 % significance level (Auchère et al., 2016) using this fitted curve as the background model. The 95 % confidence level is shown by the green curve. A green line contour defining the wavelet power map has a 95 % local significance level that was established using the power law model.

2.4.3 Cross-Wavelet analysis technique

According to Torrence and Compo (1998), the cross-wavelet transform is the result of multiplying the complex wavelet transformation of one time-series by the complex conjugate of the wavelet transformation of another time-series. To understand the physical properties underlying the oscillations in the transition area, we computed a cross-wavelet between intensity and Doppler velocity oscillations in Chapter 3 (see, Figure 2.9). The details of such cross-wavelet analysis are given in Chapter 4. By taking one example of the observed time-series, we demonstrate various features of cross wavelet spectra. In Chapter 4, we have utilized the cross-wavelet in order to determine if oscillations in the higher atmosphere, namely the chromosphere and transition region, are correlated with the oscillations in the lower atmosphere, namely the photosphere. Velocity signals of various spectral line pairs formed at different atmospheric heights are analyzed. Phase differences, cross-power, and wavelet coherence were all calculated. In the time-frequency domain, the cross-power indicates the high common power between the two signals, whereas wavelet coherence pinpoints the regions where the two signals are coherent but do not necessarily have high common power. We employ wavelet coherence to examine the synchronised oscillations between two signals. The cross-wavelet power is divided by the square root of the product of the two signals' powers to determine it. The wavelet coherence value is zero when there is no correlation between the two signals. On the other hand, a coherence value of one indicates the highest association between two signals (e.g., Bloomfield et al., 2004a; Torrence and Compo, 1998). We computed the phase differenes between two sigals by using the real and imaginary components of cross-wavelet power (Bloomfield et al., 2004a; Torrence and Compo, 1998).

All other neccessary details regarding the analysis wavelet and corss-wavelet tool are described in Chapter 3,4,and 5. Subsequently, based on the imaging and spectral observational data captured by various space-borne and ground based observatories, various

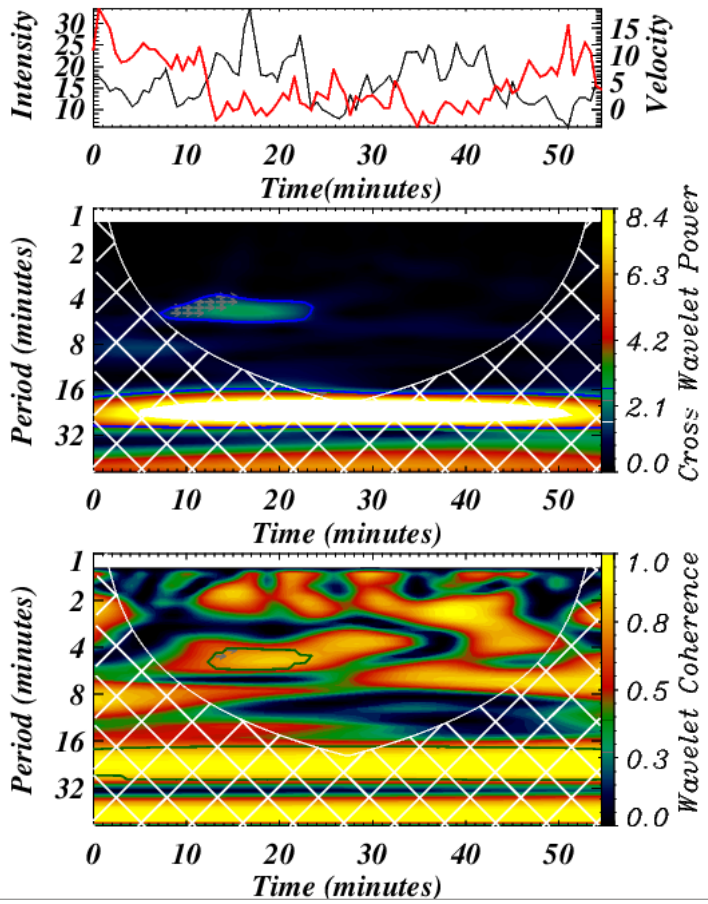

Figure 2.9: Image showing one example of the cross-wavelet. The details are given in Chapter 3.

methods and techniques are employed to determine the physical properties and dynamical processes of the emitting plasma. In the forthcoming chapter, we discuss the scientific findings on the periodicity of oscillations in the solar transition region, as well as provide insights into their physical basis using IRIS spectroscopic observations.